Tackling the Kidnapped Robot Problem via Sparse Feasible Hypothesis Sampling and Reliable Batched Multi-Stage Inference

Muhua Zhang, Lei Ma, Ying Wu, Kai Shen, Deging Huang, and Henry Leung, Fellow, IEEE

Abstract—This paper addresses the Kidnapped Robot Problem (KRP), a core localization challenge of relocalizing a robot in a known map without prior pose estimate when localization loss or at SLAM initialization. For this purpose, a passive 2-D global relocalization framework is proposed. It estimates the global pose efficiently and reliably from a single LiDAR scan and an occupancy grid map while the robot remains stationary, thereby enhancing the long-term autonomy of mobile robots. The proposed framework casts global relocalization as a non-convex problem and solves it via the multi-hypothesis scheme with batched multi-stage inference and early termination, balancing completeness and efficiency. The Rapidly-exploring Random Tree (RRT), under traversability constraints, asymptotically covers the reachable space to generate sparse, uniformly distributed feasible positional hypotheses, fundamentally reducing the sampling space. The hypotheses are preliminarily ordered by the proposed Scan Mean Absolute Difference (SMAD), a coarse beam-error level metric that facilitates the early termination by prioritizing high-likelihood candidates. The SMAD computation is optimized for non-panoramic scans. And the Translation-Affinity Scan-to-Map Alignment Metric (TAM) is proposed for reliable orientation selection at hypothesized positions and accurate final pose evaluation to mitigate degradation in conventional likelihood-field metrics under translational uncertainty induced by sparse hypotheses, as well as non-panoramic LiDAR scan and environmental changes. Real-world experiments on a resource-constrained mobile robot with non-panoramic LiDAR scan demonstrate that the proposed framework outperforms existing methods in both global relocalization success rate and computational efficiency.

Index Terms—Kidnapped robot problem, relocalization, multiple hypotheses, non-panoramic LiDAR.

I. INTRODUCTION

WITH the advancement of robotics, mobile robots are increasingly deployed in industrial environments [1], [2], [3]. Safe and efficient operation of mobile robots requires robust autonomous mapping, localization, and navigation [4], [5], [6], [7]. Mainstream localization methods include inertial odometry [8], vision-based Simultaneous Localization and Mapping (SLAM) [9], LiDAR-based SLAM, either standalone [10] or vision-augmented [11], [12], and infrastructure-based

This work was supported by the National Natural Science Foundation of China (Grants 62203371). (Corresponding author: Kai Shen).

Muhua Zhang, Lei Ma, Ying Wu, Kai Shen, Deqing Huang are with the School of Electrical Engineering, Southwest Jiaotong University, Chengdu 611756, China (e-mail: shenkai@swjtu.edu.cn).

Henry Leung is with the Department of Electrical and Computer Engineering, University of Calgary, Calgary AB T2N 1N4, Canada (e-mail: leungh@ucalgary.ca).

methods [13]. Overall, compared with vision, LiDAR-based SLAM is robust and has been widely adopted in practice [14], particularly in 2-D indoor localization tasks.

In LiDAR-based SLAM, the entire pure localization process usually happens at two stages [15]. The first is global relocalization, which provides a coarse pose estimate within the prior map and essentially corresponds to the Kidnapped Robot Problem (KRP), while the second is local refinement, enabling continuous pose tracking. Many studies aim to unify these stages. 2-D Monte Carlo Localization (MCL)-based methods [16], [17], [18], [19], [20] sample global pose hypotheses and update particle weights iteratively, expecting convergence to the correct pose. Scan-correlation-based systems such as Cartographer [21], as well as extended approaches with global matching capabilities [22], typically search candidate poses within a bounded window and apply branch-and-bound (BnB) optimization. However, when the robot remains stationary, the likelihood landscape becomes highly non-convex. The periodic alignment between the LiDAR scan and map yields multiple observation-consistent local maxima. Thus, this multimodality breaks monotonicity and prevents convergence, violating both large-sample assumptions in particle filters and the unimodality required by BnB. As a result, these methods often fail to achieve correct global relocalization when the robot is stationary. Thereby, in practice, global relocalization is often performed manually, following the paradigm of the Robot Operating System (ROS) [23], or assisted by external beacons. Consequently, when starting from an unknown pose or recovering from the localization failure, LiDAR-only mobile robots struggle to autonomously restore pose tracking, limiting long-term autonomy under minimal sensor configurations.

Many studies focus on global relocalization instead of unifying it with pose tracking in SLAM to address this challenge. Conventional methods can be categorized as active or passive. Active relocalization aims to overcome convergence issues when the robot is stationary. It extends sensor coverage through motion without prior maps, such as in-place rotation [24] or exploration guided by information gain [25], [26], [27], [28], [29]. These methods improve the chance of converging to the correct global pose but require robot motion, reducing efficiency and increasing risk in unknown environments. Passive relocalization estimates the global pose directly from observations while the robot remains stationary. It is more efficient and safer, making it an emerging research direction. A LiDAR scan descriptor for passive global relocalization is proposed in [30]. It is effective in 3-D point cloud maps but

dependent on laser intensities, which are unstable over long-term spatiotemporal evolution and unsuitable for common 2-D indoor SLAM. The 2-D method [31] compared LiDAR scan images with multi-scale map images using line and point features for pre-filtering. It further assumed a known relation between the Attitude and Heading Reference System (AHRS) heading and the map orientation to reduce the search space. However, image feature-based methods are unstable in real world complex scenes, and the orientation pruning relies on AHRS alignment that is often unavailable. Recent works sample candidate poses across the map to form a search space, then apply staged scoring and selection to progressively narrow it. The main challenges include balancing sample density and map coverage, improving robustness of scan-to-map alignment metrics, and maintaining efficiency and solution diversity in candidate selection. The related work [32] uses particle-based random sampling to generate hypothesis candidates and performs brute force search scoring on each candidate through Fourier-Mellin invariant matching. However, traditional particle sampling struggles to balance uniform coverage with sample size, and ignores traversability, producing several invalid hypotheses. The efficiency of the approach is limited when it is combined with brute force search. The work in [33] adopts a similar sampling strategy but introduces the Cumulative Absolute Error per Ray (CAER) to measure scan-to-map alignment. It uses CAER for pre-filtering and re-evaluates refined poses after registration. This improves efficiency, but for non-panoramic LiDAR scan, CAER lacks rotational invariance, requiring enumeration of orientations and beam-wise recomputation. However, staged selection based merely on coarse CAER, may still miss the correct pose.

Motivated by the above results, this paper considers a stationary mobile robot that estimates its global pose using only laser scans and a prior occupancy-grid map before continuous pose tracking. A traversability-constrained Rapidly-exploring Random Tree (RRT) under is used for positional hypothesis sampling. It provides sparse, uniform, and feasible coverage of the robot's map-embedded state space, ensuring all hypotheses are reachable. The Scan Mean Absolute Difference (SMAD) is adopted as a coarse metric between the LiDAR scan and map-synthesized scans to rank these hypotheses efficiently. Although SMAD also shows angular anisotropy under non-panoramic LiDAR Field of View (FoV) and requires orientation-wise recomputation, it can be accelerated by range prefix sums of map-synthesized scans. The Translation-affinity scan-to-map Alignment Metric (TAM) is introduced to improve the pose inference accuracy with sparse hypotheses in complex environments. TAM identifies the correct orientation under translational uncertainty and provides stable confidence estimation even in dynamic scenes. Finally, a complete relocalization pipeline based on batched processing and early termination is adopted to balance completeness and efficiency, expanding the diversity for hypothesis exploration while keeping the inference time cost tractable. The main contributions of this manuscript are as follows.

 Conventional random particle sampling for global relocalization struggles to balance sparsity and spatial

- uniformity, and may produce infeasible samples beyond the robot's reachable space. The RRT under robot traversability constraints is employed to fundamentally reduce the sampling space and accelerate relocalization. It asymptotically covers the map to generate sparse and uniformly distributed positional hypotheses, ensuring all samples lie within the robot's feasible state space.
- 2) The beam-error level metric, SMAD, is proposed for rapid evaluation of similarity between laser scan and map-synthesized scan. It is employed for preliminary hypothesis ordering, enabling candidates with higher likelihood to be prioritized and thereby allowing early termination for efficiency. For non-panoramic LiDAR, SMAD exploits the prefix sum of map-synthesized scan ranges to accelerate orientation-wise recomputations caused by angular anisotropy.
- 3) An enhanced likelihood-field scan-to-map alignment metric, TAM, is proposed for reliable orientation selection under translational uncertainty induced by sparse sampling and accurate final pose evaluation under non-panoramic scans and scene dynamics. It integrates FoV-adaptive beam retention mechanism and structural consistency term, mitigating the degradation of conventional likelihood-field-based metrics.
- 4) A batched multi-stage inference process with local top k selection and early termination is proposed to address the failure of conventional optimization in the non-convex global relocalization problem and the limited inclusiveness of optimal solutions in pruning- or BnB-based methods. It balances solution diversity and efficiency. Experimental results demonstrate that the proposed framework improves relocalization success rates and reduces runtimes compared with existing methods, providing a practical solution to KRP.

The remainder of this paper is organized as follows. Section II formulates passive global relocalization. Section III presents the proposed relocalization framework. Section IV reports real-world experiments and ablation studies. Section V gives the conclusion of the paper and potential future works.

II. PRELIMINARIES AND PROBLEM STATEMENT

A. Passive Global Relocalization

In the passive global relocalization, the robot remains stationary and infers its global pose exclusively from a LiDAR scan and an occupancy-grid map without an initial pose estimate [31], [32], [33]. Let the map be denoted by \mathcal{M} , and the free space in \mathcal{M} by $\Omega \subset \mathbb{R}^2$. The robot pose is defined as

$$\mathbf{x} = (\mathbf{p}, \theta) \in \mathbb{SE}(2), \mathbf{p} = (x, y)^T \in \Omega, \theta \in [-\pi, \pi).$$
 (1)
A single LiDAR scan is represented as

$$Z = (\phi_i, z_i)_{i=1}^{N_z}, \phi_i \in [-\pi, \pi), z_i \in \mathbb{R}^+,$$
 (2)

where N_Z is the number of beams, ϕ_i the beam angle, and z_i the corresponding range on ϕ_i .

The global relocalization process can be formulated as a maximization of a generalized evaluation function [31]:

$$x^* = \operatorname{argmax} \mathcal{F}(\mathbf{Z}, x \mid \mathbf{M}), \tag{3}$$

where \mathcal{F} outputs an alignment score between the LiDAR scan observation \mathcal{Z} and the map \mathcal{M} under a candidate pose x. \mathcal{F} is

generally designed to be implemented based on likelihood field [31] or based on beam-error level metric [33]. This problem exhibits non-convexity and multimodality. Periodic alignments between environmental structures and scan beams lead to multiple local maxima, especially under non-panoramic LiDAR FoV. Formally, there may exist a set of stationary points $\{x^{(k)}\}_{k=1}^K$ such that

$$\nabla_{x} \mathcal{F} \left(\mathcal{Z}, x^{(k)} \mid \mathcal{M} \right) = 0, \nabla_{x}^{2} \mathcal{F} \left(\mathcal{Z}, x^{(k)} \mid \mathcal{M} \right) < 0, \quad (4)$$

with

$$\mathcal{F}(\mathbf{Z}, \mathbf{x}^{(1)} \mid \mathbf{M}) \approx \mathcal{F}(\mathbf{Z}, \mathbf{x}^{(2)} \mid \mathbf{M}) \approx ... \approx \mathcal{F}(\mathbf{Z}, \mathbf{x}^{(K)} \mid \mathbf{M}). (5)$$

Consequently, this multimodal landscape violates the unimodality assumption required for effective convergence, often causing gradient-based optimization solutions to stall in local optima. This makes it difficult for global relocalization to directly use methods like Iterative Closest Point (ICP) or Normal Distributions Transform (NDT) without initial guesses.

B. Multiple Hypotheses-Based Global Relocalization

Many approaches use discretized multiple hypotheses to solve the global pose estimation problem. Based on discrete pose hypotheses, [16], [17], [18], [19], [20] use particle filter-based MCL to converge to the global pose, and [21], [22] use discrete pose search windows combined with BnB acceleration to achieve global pose registration. Particle filter-based MCL struggles in the stationary case because particles cannot diffuse via the motion model and rely only on observation likelihood. In multimodal landscapes, this causes convergence to local optima. Moreover, since BnB expands along a tree, its pruning directionality may lead to premature elimination of regions containing the true global optimum.

Recent works on global relocalization like [32], [33] combine randomly sampled position hypotheses with a set of angles enumerated at the positions to form pose hypotheses. A set of sampled positions with the sample size of N_p is generated as

$$\boldsymbol{\mathcal{P}} = \{\boldsymbol{p}_j\}_{j=1}^{N_p}, \boldsymbol{p}_j \in \Omega, \tag{6}$$

For each position p_j , the orientation is determined by solving:

$$\theta_{j}^{*} = \underset{\theta \in [-\pi,\pi)}{\operatorname{argmax}} \mathcal{F}(\mathcal{Z}, (\boldsymbol{p}_{j}, \theta) \mid \boldsymbol{\mathcal{M}}), \tag{7}$$

where the optimization can be performed either through discretized enumeration of a set of orientations or by continuous optimization over the orientation domain. The resulting pose hypothesis set \mathcal{H} can be expressed as

$$\mathcal{H} = \{ (\boldsymbol{p}_i, \theta_i^*) \}. \tag{8}$$

The global relocalization problem (3) is reformulated as selecting the best hypothesis from \mathcal{H} :

$$(\boldsymbol{p}, \theta)^* = \underset{(\boldsymbol{p}_j, \theta_j^*) \in \mathcal{H}}{\operatorname{argmax}} \mathcal{F}(\boldsymbol{Z}, (\boldsymbol{p}_j, \theta_j^*) \mid \boldsymbol{\mathcal{M}}). \tag{9}$$

A common way to construct \mathcal{P} is through fixed-amount random particle sampling. But this faces several drawbacks:

1) When N_p is small, sampling may miss the correct area or concentrate in some areas. The uneven distribution will cause \mathcal{F} to lose the global consistency of the evaluation scale.

- 2) When N_p is increased to improve hypothesis sampling coverage and uniformity, the search space increases, which leads to a fundamental increase in computational complexity
- 3) Sampled particles may lie within the free space Ω , but not within the robot's traversable set $\mathcal{R}(\boldsymbol{p}_0)$, i.e., there exists no feasible trajectory from the map origin \boldsymbol{p}_0 to the sampled position under collision constraints. Such unreachable hypotheses introduce invalid evaluations and unnecessary computational overhead.

Therefore, uniform and sparse sampling can ensure that the sampling positions are all within $\mathcal{R}(\boldsymbol{p}_0)$ and fundamentally improve computational efficiency. However, sparse sampling inevitably introduces translational error between the correct position \boldsymbol{p}^* and the nearest sampled position \boldsymbol{p}_i :

$$\Delta \boldsymbol{p}_{i} = \boldsymbol{p}^{*} - \boldsymbol{p}_{i}, \|\Delta \boldsymbol{p}_{i}\| \leq \rho, \tag{10}$$

where ρ is determined by the sampling resolution. \mathcal{F} must therefore exhibit translational affinity, i.e., it should retain orientation discriminability and pose separability even under bounded translational deviations. At the same time, in the real world, the environment often changes, and there are differences between the map and the observation. If the overall output of \mathcal{F} at the correct pose x^* degenerates to a small value, the unified threshold benchmark will become invalid, and the correct solution will be indistinguishable from the incorrect solution. Therefore, \mathcal{F} also needs to have dynamic robustness.

For the full pipeline, the global top-k pruning-selection framework used in [32], [33] scores all candidate poses and retains only the top-k hypotheses for the next round. The process iterates through several rounds of ranking and selection before producing the final solution. Compared with BnB-based search acceleration, this strategy is more advantageous in multimodal landscapes since it does not rely on a single directional pruning path which is more likely to preserve potential solutions. However, the drawback lies in its limited inclusiveness.

- 1) Due to the uncertainty of the evaluation metric caused by Δp_j , hypotheses near the correct position may rank high only among the samples with similar metric values (i.e., local top k) rather than in the global top k. If global pruning is performed, the correct solution may be mistakenly eliminated at the early stage.
- 2) The global top k selection retains a limited subset for all candidates at each stage, and the hypothesis space gradually shrinks. In highly multimodal landscapes, if the correct solution does not score prominently in the early rankings, it may not be retained.
- 3) The process inherently constructs a biased search that depends more on early ranking results than on the global structure of \mathcal{F} , which may lead to convergence toward incorrect peaks.

In summary, challenges in controlled sampling, robustness of evaluation metrics, and inclusiveness of inference pipelines remain in existing multi-hypothesis-based global relocalization methods, providing the motivation for this work.

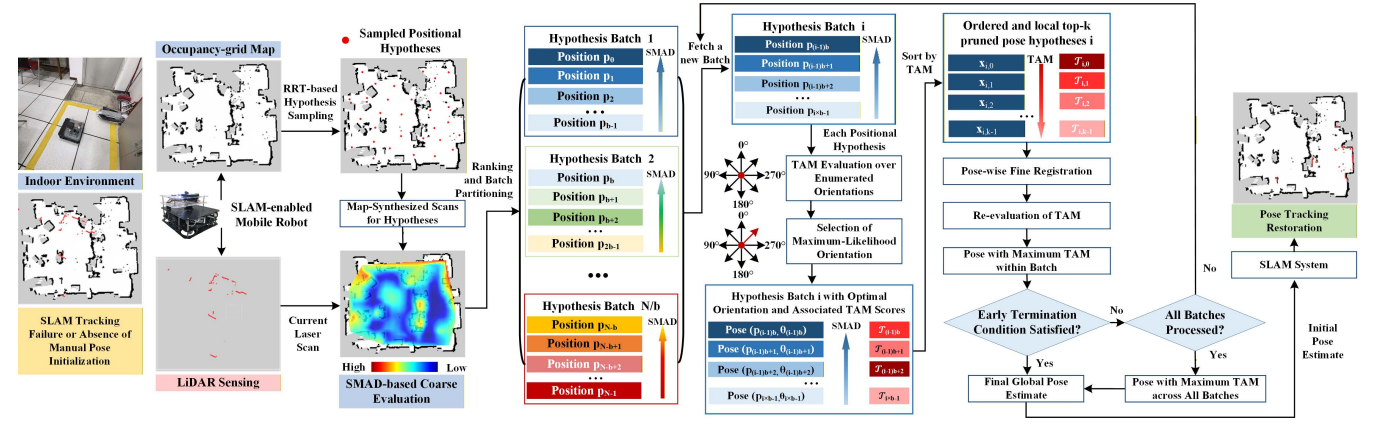


Fig. 1. The entire pipeline of the proposed framework.

Algorithm 1 Traversability-Constrained Hypothesis Sampling

Input: Map origin p_0 , RRT tree T_{RRT} , RRT sampling boundary 1: \mathcal{B} , grid map \mathcal{M} , map width $W_{\mathcal{M}}$, map height $H_{\mathcal{M}}$, map resolution $r_{\mathcal{M}}$, sampling spacing ρ , and gain threshold ε_{gain}

```
2: Output: Sparse hypotheses \mathbf{\mathcal{P}} = \{\mathbf{p}_j\}_{j=1}^{N_p} with \mathbf{p}_j \in \mathcal{R}(\mathbf{p}_0)
3: Initialize: T_{RRT} \leftarrow \{\boldsymbol{p}_0\}, \boldsymbol{\mathcal{P}} \leftarrow \emptyset, \boldsymbol{\mathcal{P}}_{last} \leftarrow \emptyset
4: N_{sampling} \leftarrow [W_{\mathcal{M}} H_{\mathcal{M}} r_{\mathcal{M}}^2 / \rho^2]
5: do
          \textbf{for } \textit{\textbf{i}} \leftarrow 1 \text{ to } N_{\textit{sampling}} \textbf{ do}
6:
7:
              p_{rand} \leftarrow Random \ point
8:
              p_{nearest} \leftarrow NearestNode(p_{rand}, T_{RRT})
9:
              \eta \leftarrow AdaptiveExpandDist(\boldsymbol{p}_{nearest}, \boldsymbol{\mathcal{M}})
10:
              p_{new} \leftarrow ExtendPoint(p_{rand}, p_{nearest}, \eta)
                               ( InSamplingBoundary ( p_{new}, B ) and
11:
                                 TraversabilityCheck(p_{nearest}, p_{new}, \mathcal{M})) then
12:
                   continue
13:
              \pmb{T}_{RRT} \leftarrow \pmb{T}_{RRT} \cup \{ \pmb{p}_{new} \}
          \mathcal{P}_{last} \leftarrow \mathcal{P}
14:
15:
          \mathcal{P} \leftarrow VoxelDownsample(T_{RRT}, \rho)
16:while |\mathcal{P} \setminus \mathcal{P}_{last}| > \varepsilon_{gain}
17:return P
```

III. PROPOSED FRAMEWORK

Fig. 1 illustrates the overall process of the proposed 2-D passive global relocalization framework. The robot starts from an unknown non-origin pose without manual initialization. The framework only takes a single LiDAR scan and an occupancy grid map as inputs. The traversability-constrained RRT first performs sparse and uniform sampling in the reachable free space to obtain global candidate positions. The beam-error level coarse metric SMAD is then used to compute the similarity between the LiDAR scan and a map-synthesized virtual scan (obtained by ray-casting the map at the positional hypothesis) for each position, rank them globally, and divide the ordered set into batches. For each batch, candidate positions are combined with enumerated orientations and evaluated using the likelihood-field-based precision alignment metric TAM. The orientation with the highest score is selected for each position, resulting in a TAM-ordered set of pose hypotheses. Top - k poses are further aligned using ICP between the LiDAR scan and the entire map, followed by re-evaluations with TAM. The system terminates early if the best re-evaluated TAM score \hat{T}_h^* exceeds a threshold τ . Otherwise, batches are

processed sequentially, and the final pose is taken as the highest-scoring hypothesis across all batches, which is then fed back to the SLAM system to resume continuous pose tracking. Remark 1: In relocalization methods using pure top -kselection [32], [33], let the correct pose be $\mathbf{x}^* = (\mathbf{p}^*, \theta^*)$, and define $\mathbf{B}^* = \{x_i : \mathcal{G}^t(x_i) \to x^*\}$ as the set of hypotheses that converge to x^* under a local refinement operator G (e.g., ICP). For any $x \in \mathcal{B}^*$, let $\mathcal{V}(x)$ denote its rank index under the discrete scoring $\mathcal{F}(\mathbf{Z}, (\mathbf{p}_j, \theta_j^*) \mid \mathbf{M})$ evaluated at discrete positions p_i with the maximum-likelihood orientation θ_i^* . Since each p_j deviates from p^* by the non-uniform offset Δp_j , we can write $\mathcal{F}(\mathbf{Z}, (\mathbf{p}_i, \theta_i^*) \mid \mathbf{M}) = \mathcal{F}(\mathbf{Z}, (\mathbf{p}^*, \theta^*) \mid \mathbf{M}) +$ $\delta(\Delta \boldsymbol{p}_i) + \varepsilon_i$, where the bias $\delta(\Delta \boldsymbol{p}_i)$ and noise ε_i vary across j. Hence, no evaluation metric on discrete hypotheses possesses strict global consistency for comparison, and the event that all convergent hypotheses are pruned, $\mathcal{E}_{drop}^{prune} = \{\min_{\mathbf{x} \in \mathbb{R}^*} r(\mathbf{x}) > k\},$ occurs with a non-negligible probability. The proposed local top - k batch inference reduces this risk by selecting the top - k hypotheses from each score-level region, thereby ensuring that x^* and its neighboring hypotheses within the same level are more likely to be explicitly evaluated before any possible early termination. The early-termination threshold τ is set according to the score levels typically observed under well-localized conditions.

Remark 2: Although the proposed pipeline does not perform aggressive pruning of the search space, its efficiency is preserved by traversability-constrained uniform sparse RRT sampling that reduces the hypothesis domain, SMAD-based ranking that prioritizes promising candidates for early termination, and TAM that provides reliable orientation selection under sparse hypotheses. Compared with sequential pure global top - k selection, the proposed pipeline is inherently parallelizable, leading to favorable time costs under efficient implementation.

A. Traversability-Constrained Hypothesis Sampling

When the hypothesis sampling process needs to maintain both randomness and traversability, RRT is an effective choice. It samples random points in the feasible space and expands along traversable directions. This balances global exploration and local connectivity. The asymptotic completeness of RRT ensures probabilistic coverage of traversable space as iterations

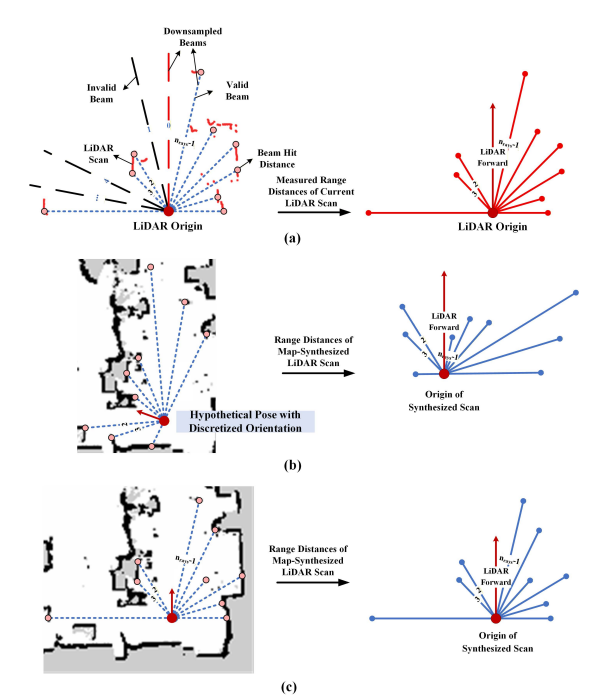


Fig. 2. Anisotropic orientation characteristic of beam-error level metrics. increase. It provides a sparse and uniformly distributed set of feasible hypotheses for global relocalization. The proposed framework uses an enhanced full-coverage RRT for positional hypothesis sampling. During node expansion, the expansion distance is adaptively adjusted based on the shortest distance between the node and nearby obstacles. The step size decreases linearly when approaching obstacles, improving exploration in narrow regions. A strict traversability check is applied. If any point along a candidate path is closer to an obstacle than the robot radius r_{robot} , the expansion is rejected to prevent unreachable hypotheses. Batched expansion and gain-based termination on downsampled nodes create an efficient stopping mechanism. This design removes the need for time-based execution to ensure coverage completeness. All RRT nodes are uniformly downsampled to generate the final set of positional hypotheses. Algorithm 1 presents the detailed process with:

- 1) NearestNode: Returns the node in T_{RRT} that minimizes the Euclidean distance to the input point p.
- 2) ExtendPoint: Generates a new point from $p_{nearest}$ toward p_{rand} with expansion distance η .
- 3) *MinDistToObstacle:* Computes the minimum Euclidean distance from the input point to the nearest occupied cell on \mathcal{M} . The distance is obtained from a precomputed lookup table built using k-d tree.
- 4) In Sampling Boundary: Checks whether the input point is within the sampling boundary \mathcal{B} , where \mathcal{B} denotes the bounding rectangle of \mathcal{M} .
- 5) AdaptiveExpandDist: Computes the adaptive expansion distance η from the input point \boldsymbol{p} according to $d_{obs} = MinDistToObstacle(\boldsymbol{p}, \boldsymbol{\mathcal{M}})$. When $d_{obs} \geq 2r_{robot}$, $\eta = \eta_{max}$, the maximum expansion distance of RRT. When $d_{obs} \leq r_{robot}$, $\eta = r_{robot}$. When $r_{robot} \leq d_{obs} \leq 2r_{robot}$, η decreases linearly as d_{obs} decreases.
- 6) TraversabilityCheck: Verifies whether all points p on the line segment $[p_0, p_1]$ satisfy $d_{obs}(p) \ge r_{robot}$.

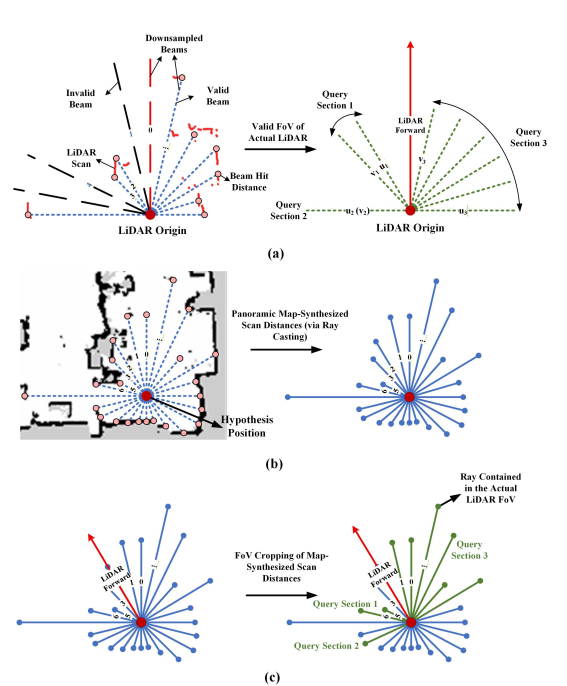


Fig. 3. Accelerated SMAD calculation via prefix sum of ranges from the panoramic map-synthesized scan.

Returns true if traversable, otherwise false.

7) *VoxelDownsample:* Performs voxel downsampling in [34] of T_{RRT} with sampling spacing ρ .

Remark 3: When the entire map \mathcal{M} is traversable, the number of representative points required for full coverage at sampling spacing ρ is $N_{sampling} = [W_{\mathcal{M}} H_{\mathcal{M}} r_{\mathcal{M}}^2/\rho^2]$. Utilizing $N_{sampling}$ expansion attempts per iteration matches the density of complete coverage, ensuring sufficient exploration intensity. The incremental coverage for the t^{th} iteration is defined as $gain(t) = |\mathcal{P}^{(t)} \setminus \mathcal{P}^{(t-1)}|$. When $gain(t) \leq \varepsilon_{gain} \to 0$, the probability of newly sampled points hitting uncovered regions approaches zero, indicating saturation of coverage over $\mathcal{R}(\boldsymbol{p}_0)$. A small positive ε_{gain} maintains completeness while avoiding stochastic termination instability. This mechanism achieves adaptive control of coverage across arbitrary map scales and sampling spacing, realizing asymptotic quasi-completeness of coverage without explicit dependence on sampling duration.

B. Beam-Error Level Coarse Metric SMAD

Beam-error metrics compute per-beam distance errors to assess consistency between LiDAR scans. For each pose hypothesis, a map-synthesized scan is generated by ray casting on the occupancy grid map. Comparing it with the actual scan yields a score that reflects the proximity of the hypothesis to the correct pose [33]. Unlike likelihood-field metrics, beam-error level metrics are computationally efficient, numerically stable, and directly correlated with range measurements, eliminating the need for normalization. They are suitable for fast evaluation over large hypothesis spaces. Although multiple high-response hypotheses may occur, their efficiency enables effective preliminary ordering, allowing hypotheses near the correct pose to be prioritized for early termination. However, for the non-panoramic LiDAR, beam-error level metrics exhibit orientation anisotropy. The FoV of the map-synthesized scan must match that of the real LiDAR. Panoramic LiDAR

maintains rotational invariance since it can cover the full scene regardless of orientation. In contrast, as shown in Fig. 2(a), non-panoramic scan only observes a partial region of the panoramic scan, and this visible region changes with orientation, as shown in Fig. 2(b) and Fig. 2(c). Thus, even for the same position, the beam set varies with orientation, introducing anisotropy. For such LiDAR scan, beam subsets must be reselected, and the metric recomputed across discrete orientations, which increases computational cost.

To address the efficiency issue, the proposed SMAD is defined as the absolute value of the difference between the average ranges of two scans. This allows for acceleration by prefixing the sum of the ranges of beams in map-synthesized scan. SMAD uses downsampled scan, which is represented as

$$\mathbf{Z}' = (\phi_i', z_i')_{i=1}^{N_Z'}, \phi_i' = \phi_{i \cdot n_{skip}^{beam}}, \tag{11}$$

where n_{skip}^{beam} is the scan sampling stride. Because of LiDAR FoV limitation and invalid returns, the valid beams form several disjoint continuous sections, with a total number of K:

$$Q_{FOV} = \{ I_k = [u_k, v_k] \}_{k=1}^K, I_k \cap I_{k'} = \emptyset, k \neq k', \qquad (12)$$

Each I_k represents a section of consecutive valid beams, as shown in Fig. 3(a). At a positional hypothesis $p \in \mathcal{R}(p_0)$, a panoramic map-synthesized scan is generated by ray casting, as shown in Fig. 3(b):

$$\widehat{\mathbf{Z}}'(\mathbf{p}) = \{\widehat{z}_i'(\mathbf{p})\}_{i=1}^{N_S},\tag{13}$$

where N_s is the total number of beams. It can be determined by the LiDAR angular resolution $\Delta \phi$ and n_{skip}^{beam} :

$$N_s = \frac{2\pi}{\Delta\phi \cdot n_{skip}^{beam}}. (14)$$

This ensures one-to-one index correspondence between real and synthesized beams. For non-panoramic LiDAR, multiple orientations are enumerated for each positional hypothesis, and the minimum SMAD value among them is taken as the final SMAD score. LiDAR forward orientations Θ are enumerated by shifting beam indices over the panoramic scan:

$$\Theta = \{\theta_m | \theta_m = m(\Delta \phi \cdot n_{skip}^{beam})\}, \tag{15}$$

where $m = \{0, n_{skip}^{enum}, n_{skip}^{enum}, 2n_{skip}^{enum}, \dots, N_s - 1\}$, and n_{skip}^{enum} is the orientation enumerating stride. Each LiDAR orientation θ_m corresponds to an integer offset m. And orientation rotation can be achieved by shifting of m.

The mean range of the actual scan is computed once:

$$\bar{z}' = \frac{1}{\sum_{k} |I_{k}|} \sum_{k=1}^{K} \sum_{i \in I_{k}} z'_{i}.$$
 (16)

For the map-synthesized scan, define the cyclically extended prefix-sum array:

$$S[t] = \sum_{i=1}^{t} \hat{z}'_{i}(\mathbf{p}), t \in [1,2N_{s}],$$
 (17)

where $\{\hat{z}'_j(p)\}$ is duplicated once to form the cyclic extension. Then, the mean range of the synthesized scan under orientation θ_m is computed in constant time, as shown in Fig. 3(c), as

$$\bar{z}'_{syn}(\boldsymbol{p}, \theta_m) = \frac{1}{\sum_k |\boldsymbol{I}_k|} \sum_{k=1}^K (S[v_k + m] - S[u_k + m - 1]). (18)$$

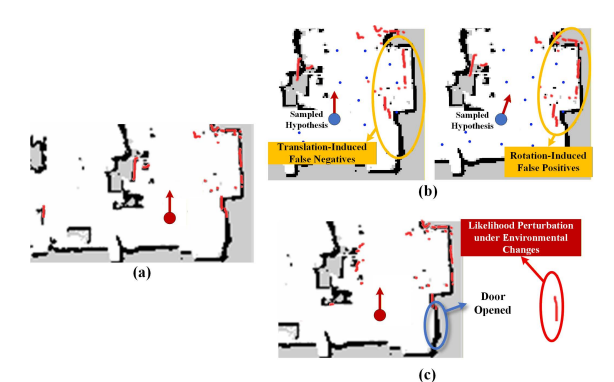


Fig. 4. Typical degradation cases of likelihood-field-based scan-to-map alignment metrics for relocalization tasks.

Finally, the SMAD at orientation θ_m is defined as

$$SMAD(\boldsymbol{p}, \theta_m) = |\bar{z}' - \bar{z}'_{svn}(\boldsymbol{p}, \theta_m)|. \tag{19}$$

And the final SMAD score can be expressed as

$$SMAD(\mathbf{p}) = \begin{cases} SMAD(\mathbf{p}, \theta_0), & (\sum_{k} |\mathbf{I}_k|)/N_s \ge 0.9 \\ \min_{\theta_m \in \Theta} SMAD(\mathbf{p}, \theta_m), \text{ otherwise} \end{cases} (20)$$

Remark 4: In [33], the CAER is defined as

$$CAER(\boldsymbol{p}, \theta_m) = \frac{1}{\sum_k |\boldsymbol{I}_k|} \sum_{k=1}^K \sum_{i \in \boldsymbol{I}_k} |z_i' - \hat{z}_{i+m}'(\boldsymbol{p})|.$$
 (21)

Because the absolute operator lies inside the summation, prefix-sum queries cannot be applied, resulting in $O(\sum_k |I_k|)$ complexity. In contrast, SMAD only depends on mean distance differences. With one $O(N_s)$ preprocessing step for prefix sums, each section query is O(1), achieves lower complexity for non-panoramic LiDAR scan without rotation-invariant.

C. Translation-Affinity Alignment Metric TAM

For accurate scan-to-map alignment evaluation under a given pose hypothesis in localization or relocalization tasks, likelihood-field-based metrics are commonly used [16], [20], [31]. These metrics are based on the distance from each LiDAR beam endpoint to the nearest occupied cell on the grid map. Likelihood field-based metrics have higher sensitivity to alignment inconsistencies and are more scalable, making them more suitable for customized accurate alignment evaluation. Thus, in the proposed framework, the likelihood-field-based metric is applied in three stages. It first searches for the optimal orientation for each positional hypothesis to generate pose hypotheses (corresponding to the objective of (7)). It then provides the ranking basis for pose hypotheses. Finally, it evaluates the alignment score of refined poses after registration (corresponding to the objective of (9)). (7) is implemented in a discrete form as follows:

$$\theta_{j}^{*} = \underset{\theta_{m} \in \Theta}{\operatorname{argmax}} \, \mathcal{F}\left(\mathcal{Z}', (\boldsymbol{p}_{j}, \theta_{m}) \mid \boldsymbol{\mathcal{M}}\right). \tag{22}$$

However, for orientation selection tasks under sparse positional hypothesis sampling and pose evaluation in complex real-world environments, the traditional likelihood-field-based metric [16], [31] tends to degrade. As shown in Fig. 4(a), under ideal conditions, the geometric correspondence between the scan and the map produces high-scoring alignment responses. When the positional hypothesis has a significant translational deviation Δp_i from the correct position, as shown in Fig. 4(b), the laser

beams with the correct orientation become globally misaligned with structural boundaries and yield lower likelihood scores than incorrect orientations. This is translation-induced metric degradation. In real-world scenarios, even small-scale dynamic changes such as an opened door can cause local inconsistencies between the scan and the scene. As shown in Fig. 4(c), when the pose is correct, these local mismatches can sharply reduce the likelihood response. The local likelihood perturbation becomes more significant when the scan is non-panoramic.

To address the above issues, TAM is proposed. It possesses robustness in dynamic environments and maintains sensitivity to orientation estimation even in the presence of translational offsets, thereby exhibiting translation affinity. Let the hypothesized robot pose be denoted as x. Each scan beam endpoint of Z' in the map coordinate frame is represented by $q_i(x)$. The likelihood-field model is defined as

$$\ell_i(\mathbf{x}) = \log(z_{hit} exp(-\frac{d_{obs}^2(q_i(\mathbf{x}))}{2\sigma_{hit}^2}) + z_{rand} + \varepsilon), \quad (23)$$

where z_{hit} is the weight of the hit component, which represents the probability that a beam endpoint coincides with the obstacle, σ_{hit} controls the spatial decay of the likelihood field, z_{rand} is the weight of the random measurement term, used to model unstructured noise, and $\varepsilon = 1e^{-6}$ is a small constant added for numerical stability. In dynamic environments, some beams yield abnormally low likelihood responses. Retaining these unstable beams can dominate the alignment statistics and excessively lower the matching score. To address this, TAM introduces a FoV-adaptive beam retention mechanism that balances information completeness and robustness across different FoV configurations. All beam responses are sorted in descending order:

$$\ell_1(\mathbf{x}) \ge \ell_2(\mathbf{x}) \ge \dots \ge \ell_{N_{\alpha}'}(\mathbf{x}). \tag{24}$$

Let the ratio of the actual LiDAR FoV to the panoramic FoV $\lambda = \frac{\sum_k |I_k|}{N_S}$, three retention ratios are defined as

$$\begin{cases} \alpha_{full} = 1 \\ \alpha_{mid} = \alpha_{mid}^{min} + \lambda(\alpha_{mid}^{max} - \alpha_{mid}^{min}), \\ \alpha_{low} = \alpha_{low}^{min} + \lambda(\alpha_{low}^{max} - \alpha_{low}^{min}) \end{cases}$$
(25)

with $\alpha_{full} > \alpha_{mid} > \alpha_{low}$. A larger FoV removes more low-likelihood beams to suppress unstable responses, while a smaller FoV retains more beams to preserve observation completeness. The corresponding beam numbers are

$$k_{full} = N_Z', k_{mid} = \lfloor \alpha_{mid} N_Z' \rfloor, k_{low} = \lfloor \alpha_{low} N_Z' \rfloor,$$
 (26) and the final robust response is obtained by

$$\bar{\mathcal{L}}(x) = med\{\frac{1}{k_{full}} \sum_{i=1}^{k_{full}} \ell_i, \frac{1}{k_{mid}} \sum_{i=1}^{k_{mid}} \ell_i, \frac{1}{k_{low}} \sum_{i=1}^{k_{low}} \ell_i\}. \quad (27)$$

This adaptive filtering balances full, moderate, and strong exclusion modes. It enables TAM to automatically adjust to FoV variations and maintain stable alignment responses in dynamic or partially changed environments. Based on the robust likelihood response, the alignment likelihood term is defined as

$$p(x) = exp(\bar{\mathcal{L}}(x)), \tag{28}$$

which represents the overall matching probability between the scan and the map structure. However, relying solely on the likelihood response makes stable normalization difficult. Because of the exponential decay of the likelihood-field model, even a few unmatched beams can cause a sharp decrease in the overall score. This makes the metric highly sensitive to local mismatches. To mitigate this effect, TAM introduces geometric distance statistics to complement the likelihood measure. After calculating the mean and variance of all distances $d_{obs}(q_i(x))$, $\bar{d}(x)$ and $\hat{\sigma}^2(x)$ are obtained. Here, $\bar{d}(x)$ reflects the average proximity of the scan to structural boundaries, and $\hat{\sigma}^2(x)$ reflects the consistency of distance distribution. To eliminate the influence of resolution and scale, the mean distance is clamped and normalized. Let the maximum valid distance be d_{max} and the minimum effective distance be $d_{min} = r_{\mathcal{M}}/2$:

$$\tilde{d}(\mathbf{x}) = \min(\max(\bar{d}(\mathbf{x}), d_{\min}), d_{\max}),$$

$$s_d(\mathbf{x}) = 1 - \frac{\tilde{d}(\mathbf{x}) - d_{\min}}{d_{\max} - d_{\min}} \in [0, 1].$$
(29)

The term $s_d(x)$ provides a smooth geometric correction to the likelihood response. It linearly maps the average distance into [0,1], suppressing rapid likelihood decay caused by local mismatches and improving continuity and comparability across environments. However, both p(x) and $s_d(x)$ remain strongly dependent on absolute distance magnitude. When a fixed translational offset exists between the hypothesized and correct positions, this dependency biases the score toward distance magnitude rather than geometric consistency. Such bias reduces translation affinity and hinders accurate orientation evaluation and global consistency of the metric. To address this issue, TAM introduces the structural consistency term:

$$c(x) = exp(-\frac{1}{2}\hat{\sigma}^2(x)),$$
 (30)

which measures the structural stability of distance distribution. When a translational offset exists but the orientation is correct, each term $d_{obs}(\mathbf{q}_i(\mathbf{x}))$ remains approximately equal to the translation magnitude. In this case, the variance $\hat{\sigma}^2(\mathbf{x})$ stays small, leading to an increase in $c(\mathbf{x})$. This compensates for the reduction of $p(\mathbf{x})$ and $s_d(\mathbf{x})$, thereby achieving translation affinity of the metric. Finally, the three components are fused through geometric averaging to obtain the normalized TAM:

$$\mathcal{T}(x) = (p(x)s_d(x)c(x))^{\frac{1}{3}} \in (0,1].$$
 (31)

Remark 5: In [31], the traditional likelihood-field-based scan-to-map alignment metric is simply defined as

$$p_{LF}(\mathbf{x}) = \sum_{i=1}^{N_Z'} \ell_i(\mathbf{x}). \tag{32}$$

The lack of normalization causes the metric values to depend strongly on the number of beams and the overall distance scale. This dependency prevents global comparability across different pose hypotheses. When sparse positional hypothesis sampling produces translational deviations, as shown in Fig. 4(b), the scan becomes globally misaligned with the map boundaries. Though the correct orientation preserves geometric consistency, its mean distance to occupied cells increases, resulting in a lower likelihood score than that of incorrect orientations. This leads to translation-induced degradation of the metric. The proposed TAM mitigates these issues by introducing a structural consistency term and a normalization strategy based on the geometric mean.

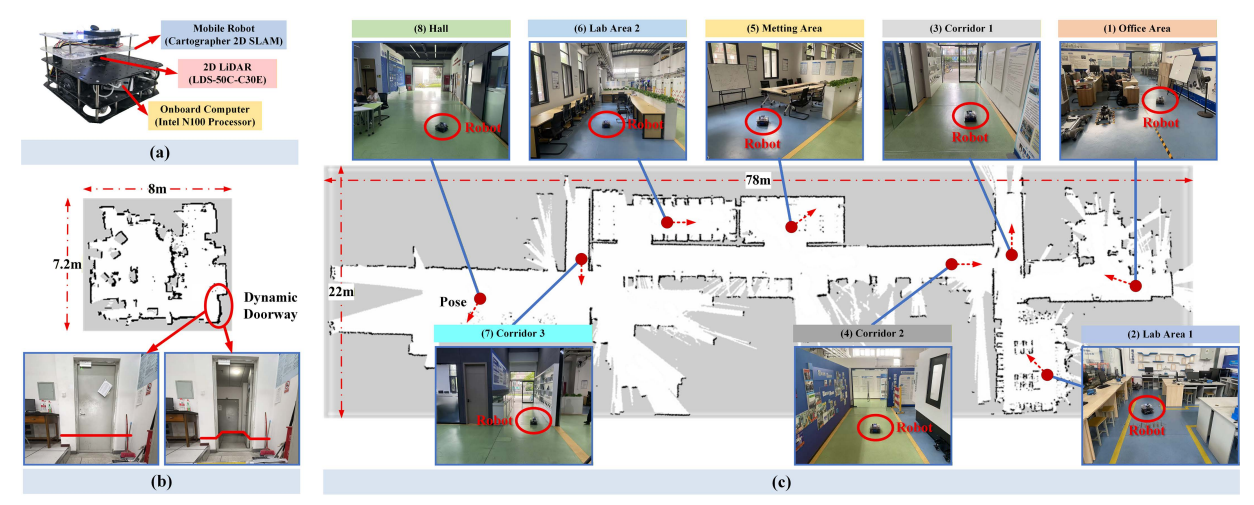


Fig. 5. Experimental robot and configurations of real-world experimental scenarios.

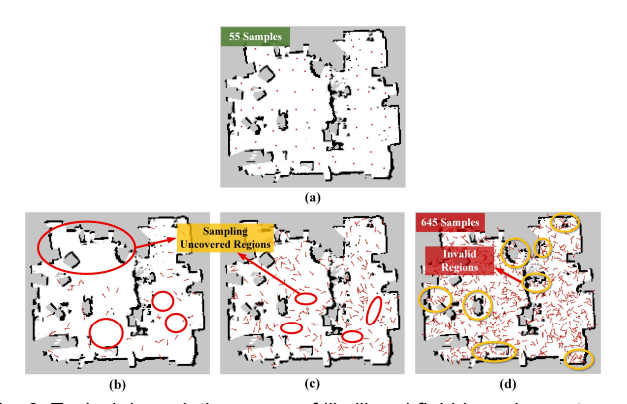


Fig. 6. Typical degradation cases of likelihood-field-based scan-to-map alignment metrics for relocalization tasks.

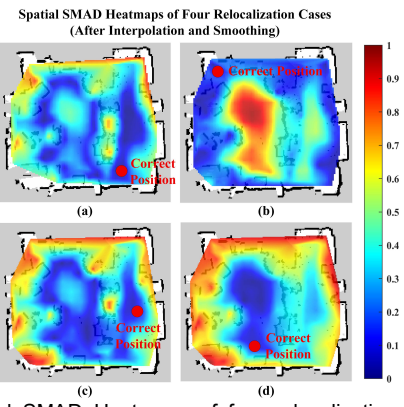


Fig. 7. Spatial SMAD Heatmaps of four relocalization cases in the scenario of Fig. 5(b).

IV. EXPERIMENTS

A. Experimental Setup

Fig. 5 shows the experimental setup. The platform is a low-cost differential-drive robot equipped with an Intel N100 embedded processor (with four E-cores) running Ubuntu 20.04, as shown in Fig. 5(a). A Bluesea LDS-50C-C30E 2-D LiDAR is used, with the set effective range of 20m, the set valid FoV of 220° , and the radius of the robot $r_{robot} = 0.21m$.

To evaluate the effectiveness of the proposed passive 2-D global relocalization framework, three sets of experiments were conducted, as described below. A demo video showcasing the

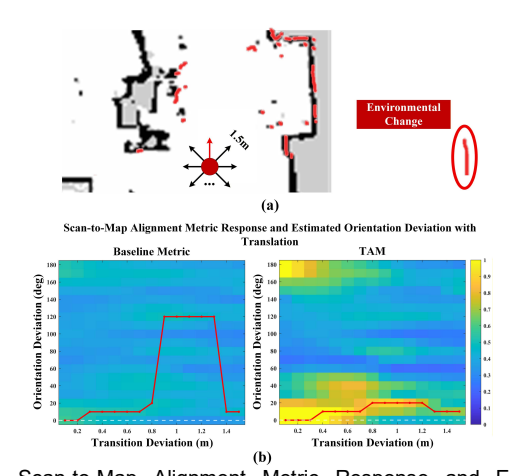


Fig. 8. Scan-to-Map Alignment Metric Response and Estimated Orientation Deviation with Translation (Normalized Likelihood vs TAM). relocalization performance of the proposed framework is available at https://youtu.be/knsAm4b5_Cc.

Case 1: Functional validation of core parts. The small and cluttered environment in Fig. 5(b) was used to validate the core parts of the framework. Specifically, the experiments validated the sparse full-coverage hypothesis sampling capability of the traversability-constrained RRT, the inclusion of the SMAD of the correct position, and the discriminative capability of TAM under translational uncertainty and environmental changes.

Case 2: Comparative evaluations of overall relocalization pipeline. In the larger industrial-like scenario shown in Fig. 5(c), the proposed framework was compared with two advanced baselines, GMCL [17] and CBGL [33]. Eight representative poses were first recorded under valid SLAM tracking (using Cartographer 2-D) and marked on the floor. After initialization at the map origin, the robot was "kidnapped" to these poses in random order for relocalization using both baselines and the proposed method. The estimated poses were compared with the SLAM-tracked ground truth. All methods were evaluated for success rates, efficiency, and pose accuracy.

Case 3: Ablation studies within the proposed framework. First, an ablation study was conducted on SMAD. Three configurations were tested without SMAD ordering, with SMAD ordering but without prefix-sum acceleration, and with both SMAD ordering and prefix-sum acceleration. The same

TABLE I. EVALUATIONS OF GLOBAL RELOCALIZATION METHODS

Daga	GMCL-8000				CBGL- D 15				Proposed- D1			
Pose	SR (%)	$t_{avg}(s)$	d_{avg}^{err} (s)	φ_{avg}^{err} (°)	SR (%)	$t_{avg}(s)$	d_{avg}^{err} (s)	φ_{avg}^{err} (°)	SR (%)	$t_{avg}(s)$	d_{avg}^{err} (s)	φ_{avg}^{err} (°)
1	50	16.891	0.077	3.713	90	3.156	0.051	1.883	95 (↑)	0.466 (↓)	0.061	1.577
2	35	28.817	0.058	2.684	10	3.192	0.085	2.819	85 (↑)	1.597 (\psi)	0.057	2.734
3	0	/	/	/	40	2.853	0.076	3.001	80 (↑)	0.992 (\psi)	0.041	1.216
4	0	/	/	/	0	/	/	/	10 (↑)	1.533	0.045	1.347
5	10	18.648	0.063	3.176	90	3.101	0.069	2.245	100 (†)	0.901 (\psi)	0.058	0.958
6	30	24.101	0.081	2.985	95	2.899	0.078	2.673	95	0.899 (\1)	0.096	0.841
7	0	/	/	/	35	2.596	0.093	2.118	100 (†)	0.726 (\psi)	0.089	2.493
8	5	27.005	0.094	2.012	0	/	/	/	100 (↑)	0.613 (1)	0.023	1.002

TABLE II. ABLATION STUDY ON SMAD

ρ	SMAD Enabled	Prefix-Sum Acceleration	t_{avg} (s)
	No	No	3.106
1.0	Yes	No	1.271
	Yes	Yes	0.966 (1)

relocalization procedure as in Case 2 was applied. Since the overall success rates of the three configurations were similar due to the batched processing mechanism, the average runtime across all eight poses and repetitions were computed to verify the efficiency gain from SMAD ordering and prefix-sum acceleration. An ablation study was performed on the TAM module. The baseline metric is defined as

$$p_{baseline}(\mathbf{x}) = \left(exp(\frac{p_{LF}(\mathbf{x})}{N_Z'})s_d(\mathbf{x})\right)^{\frac{1}{2}} \in (0,1], \quad (33)$$

representing a normalized likelihood-field metric without the FoV-adaptive beam retention mechanism or the structural consistency term. Using TAM and $p_{baseline}$ respectively, the same relocalization procedure as in Case 2 was executed. The average success rate and average runtime across all eight poses and repetitions were calculated to evaluate the effectiveness of TAM in improving relocalization performance.

B. Functional Validation of Core Parts

Fig. 6 compares the proposed traversability-constrained RRT sampling with random particle sampling for generating positional hypotheses. With a sampling spacing of $\rho=1.0m$, corresponding to an expected hypothesis density of $\mathcal{D}=1m^{-2}$, the proposed method achieves uniform and sparse coverage within the traversable region $\mathcal{R}(\boldsymbol{p}_0)$, as shown in Fig. 6(a), with $\varepsilon_{gain}=2$ and $\eta_{max}=0.6m$. For random sampling, varying \mathcal{D} controls the total number of samples. At $\mathcal{D}=1$ and $\mathcal{D}=5$, many uncovered areas remain, as shown in Fig. 6(b) and Fig. 6(c). When $\mathcal{D}=15$, the coverage improves, as shown in Fig. 6(d), but the number of samples grows excessively, and many lie outside $\mathcal{R}(\boldsymbol{p}_0)$, reducing subsequent search efficiency.

Fig. 7 shows spatial SMAD distributions for four different robot positions during relocalization. $n_{skip}^{beam}=4$. Regions with low SMAD values, indicating high scan-map consistency, are not unique, demonstrating the coarse nature of beam-error level metrics. However, the correct positions lie within low-SMAD regions. This demonstrates that after SMAD ranking, hypotheses near the correct positions are prioritized in early batches, improving overall relocalization efficiency.

Fig. 8 shows likelihood-field based scan-to-map metrics under translation and environmental changes. The scenario in Fig. 8(a) includes the door-opening variation of Fig. 5(b). Using 10° angular and 0.1m translational steps, 540 test poses

TABLE III. ABLATION STUDY ON TAM

ρ	Metric	SR (%)	$t_{avg}(s)$
1.0	$p_{baseline}(x)$	18	0.794
1.0	TAM	83	0.966
0.5	$p_{baseline}(x)$	68	1.605
0.5	TAM	84	1.723

were generated from the correct pose in Fig. 8(a). $z_{hit} = 1.0$, $\sigma_{hit} = 0.2$, and $z_{rand} = 0$. Both the $p_{baseline}$ and TAM were computed for all hypotheses. As shown in Fig. 8(b), the heatmaps illustrate metric values, and the red curves indicate the orientation deviation of the maximum response for each translation. TAM remains stable with smaller orientation errors under translation. In addition, $p_{baseline}$ degrades notably under environmental changes.

C. Comparative Evaluations of Global Relocalization

The overall relocalization experiments were conducted at eight poses shown in Fig. 5(c). Each method was repeated twenty times with the visiting order of poses randomized. For GMCL, the particle number was set to 8000, which is the empirical upper limit to prevent long particle-update stalls during computation, and other parameters followed the default settings. Global relocalization was attempted by repeatedly triggering in-place particle updates with a 30s time limit. Timeouts were considered failures. For CBGL and the proposed framework, full relocalization was executed directly. A relocalization was considered successful when positional error $d_{err} < 0.5m$ and angular error $\phi_{err} < 30^{\circ}$, which is sufficient for pose tracking initialization in Cartographer. In CBGL, $n_{skip}^{beam} = 4$. For both CBGL and the proposed framework, the number of orientation samples in (22) is set to 32. Following Case 2, CBGL used $\mathcal{D} = 15$, and the proposed framework used $\mathcal{D} = 1$. For proposed framework, each batch contains 200 hypotheses, and the local top - 20 are retained. The early-termination threshold $\tau = 0.95$. Other parameters followed Case 2 configurations. As shown in Table I, the proposed framework achieved higher overall success rates (SR) and lower average runtimes than both baselines.

D. Ablation Studies

Tables II and III summarize the ablation results. Table II shows that SMAD ranking significantly improves the efficiency of the batched multi-stage pose inference with early termination, while prefix-sum acceleration further reduces the average runtime by about 24%. Table III shows that TAM slightly increases computation cost but achieves much higher relocalization success rates than $p_{baseline}$. Moreover, with sampling at $\rho=1.0$, TAM attains a success rate comparable to that at $\rho=0.5$, demonstrating its affinity to translational uncertainty under sparse sampling.

V. CONCLUSION

This paper presents a passive 2-D LiDAR-based global relocalization framework, aiming to tackle the kidnapped robot problem. By integrating traversability-constrained RRT-based hypothesis sampling, SMAD-based coarse ranking, TAM for orientation selection and precise scan-to-map evaluation, and batched multi-stage inference with early termination, the proposed framework achieves a balance between reliability and efficiency. Real-world experiments in industrial-like scenarios verify its enhanced relocalization success rate and reduced computation time compared with existing approaches. This improves the long-term autonomous robustness of mobile robots. For future works, we will focus on improving the robustness in repetitive and low-feature environments. We also plan to improve the multi-robot global relocalization capability based on inter-robot constraints when multiple robots are present, resulting in further obstruction of LiDAR FoV.

REFERENCES

- Q. Tang, L. Ma, Y. Sun, G. Yang, Z. Li and D. Zhao, "A Heuristic Path Planning Algorithm for Inspection Robots," 2020 39th Chinese Control Conference (CCC), Shenyang, China, 2020, pp. 3834-3839.
- [2] M. Zhang, L. Ma, K. Shen and Y. Sun, "Graph-Based SLAM for Under-Train Inspection Robots in Narrow Site," 2024 30th International Conference on Mechatronics and Machine Vision in Practice (M2VIP), Leeds, United Kingdom, 2024, pp. 1-5.
- [3] J. Cheng, M. Zhang, L. Ma, H. Chen, Y. Gan and D. Huang, "A Hybrid-Dimensional Laser SLAM Framework for Indoor Quadruped Inspection Robots," in *IEEE Sensors Journal*, vol. 24, no. 10, pp. 16935-16942, 15 May15, 2024.
- [4] J. A. Placed et al., "A Survey on Active Simultaneous Localization and Mapping: State of the Art and New Frontiers," in *IEEE Transactions on Robotics*, vol. 39, no. 3, pp. 1686-1705, June 2023.
- [5] D. K. Lee, J. M. Pak, P. Shi and C. K. Ahn, "Finite Memory-Simultaneous Localization and Calibration With Application to Mobile Robots," in *IEEE Transactions on Industrial Electronics*, vol. 72, no. 6, pp. 6145-6154, June 2025.
- [6] W. Zhu and M. Hayashibe, "A Hierarchical Deep Reinforcement Learning Framework With High Efficiency and Generalization for Fast and Safe Navigation," in *IEEE Transactions on Industrial Electronics*, vol. 70, no. 5, pp. 4962-4971, May 2023.
- [7] M. Zhang, L. Ma, Y. Wu, K. Shen, Y. Sun and H. Leung, "High-Traversability and Precise Navigation for Mobile Robots in Constrained Environments," in *IEEE Sensors Journal*, vol. 25, no. 12, pp. 22815-22826, 15 June15, 2025.
- [8] F. Guo, H. Yang, X. Wu, H. Dong, Q. Wu and Z. Li, "Model-Based Deep Learning for Low-Cost IMU Dead Reckoning of Wheeled Mobile Robot," in *IEEE Transactions on Industrial Electronics*, vol. 71, no. 7, pp. 7531-7541, July 2024.
- [9] C. Zhai, M. Wang, Y. Yang and K. Shen, "Robust Vision-Aided Inertial Navigation System for Protection Against Ego-Motion Uncertainty of Unmanned Ground Vehicle," in *IEEE Transactions on Industrial Electronics*, vol. 68, no. 12, pp. 12462-12471, Dec. 2021.
- [10] F. Xie and S. Schwertfeger, "Robust Lifelong Indoor LiDAR Localization Using the Area Graph," in *IEEE Robotics and Automation Letters*, vol. 9, no. 1, pp. 531-538, Jan. 2024.
- [11] N. Zimmerman, T. Guadagnino, X. Chen, J. Behley and C. Stachniss, "Long-Term Localization Using Semantic Cues in Floor Plan Maps," in IEEE Robotics and Automation Letters, vol. 8, no. 1, pp. 176-183, Jan. 2023.
- [12] N. Zimmerman, L. Wiesmann, T. Guadagnino, T. Läbe, J. Behley and C. Stachniss, "Robust Onboard Localization in Changing Environments Exploiting Text Spotting," 2022 IEEE/RSJ International Conference on Intelligent Robots and Systems (IROS), Kyoto, Japan, 2022, pp. 917-924.
- [13] A. R. Jiménez Ruiz and F. Seco Granja, "Comparing Ubisense, BeSpoon, and DecaWave UWB Location Systems: Indoor Performance Analysis," in *IEEE Transactions on Instrumentation and Measurement*, vol. 66, no. 8, pp. 2106-2117, Aug. 2017.
- [14] W. P. N. dos Reis and O. Morandin Junior, "Sensors applied to automated guided vehicle position control: A systematic literature review," *The*

- International Journal of Advanced Manufacturing Technology, vol. 113, no. 1, pp. 21–34, 2021.
- [15] H. Gao, Q. Qiu, H. Liu, D. Liang, C. Wang and X. Zhang, "ERPoT: Effective and Reliable Pose Tracking for Mobile Robots Using Lightweight Polygon Maps," in *IEEE Transactions on Robotics*, vol. 41, pp. 3799-3819, 2025.
- [16] F. Dellaert, D. Fox, W. Burgard and S. Thrun, "Monte Carlo localization for mobile robots," *Proceedings 1999 IEEE International Conference on Robotics and Automation (Cat. No.99CH36288C)*, Detroit, MI, USA, 1999, pp. 1322-1328 vol.2.
- [17] I. Hatem and M. A. A. Khalil, "Development of a new technique in ROS for mobile robots localization in known-based 2D environments," Tishreen Univ. J. Res. Sci. Stud. Eng. Sci. Ser., vol. 43, pp. 1–19, 2021.
- [18] M. -A. Chung and C. -W. Lin, "An Improved Localization of Mobile Robotic System Based on AMCL Algorithm," in *IEEE Sensors Journal*, vol. 22, no. 1, pp. 900-908, 1 Jan.1, 2022.
- [19] H. Kuang, X. Chen, T. Guadagnino, N. Zimmerman, J. Behley and C. Stachniss, "IR-MCL: Implicit Representation-Based Online Global Localization," in *IEEE Robotics and Automation Letters*, vol. 8, no. 3, pp. 1627-1634, March 2023.
- [20] X. Xu et al., "Research on Mobile Robot Localization Method Based on Adaptive Motion Model and Double-Threshold Relocation Strategy," in IEEE Transactions on Instrumentation and Measurement, vol. 74, pp. 1-12, 2025.
- [21] W. Hess, D. Kohler, H. Rapp and D. Andor, "Real-time loop closure in 2D LIDAR SLAM," 2016 IEEE International Conference on Robotics and Automation (ICRA), Stockholm, Sweden, 2016, pp. 1271-1278.
- [22] J. Yang, H. Li, D. Campbell and Y. Jia, "Go-ICP: A Globally Optimal Solution to 3D ICP Point-Set Registration," in *IEEE Transactions on Pattern Analysis and Machine Intelligence*, vol. 38, no. 11, pp. 2241-2254, 1 Nov. 2016.
- [23] "rviz/UserGuide," ROS Wiki, last modified Aug. 31, 2020. [Online]. Available: https://wiki.ros.org/rviz/UserGuide. Accessed: Sep. 30, 2025.
- [24] S. -Y. An and J. Kim, "Extracting Statistical Signatures of Geometry and Structure in 2D Occupancy Grid Maps for Global Localization," in *IEEE Robotics and Automation Letters*, vol. 7, no. 2, pp. 4291-4298, April 2022
- [25] M. Seiz, P. Jensfelt and H. I. Christensen, "Active exploration for feature based global localization," *Proceedings. 2000 IEEE/RSJ International Conference on Intelligent Robots and Systems (IROS 2000) (Cat. No.00CH37113)*, Takamatsu, Japan, 2000, pp. 281-287 vol.1.
- [26] P. Jensfelt and S. Kristensen, "Active global localization for a mobile robot using multiple hypothesis tracking," in *IEEE Transactions on Robotics and Automation*, vol. 17, no. 5, pp. 748-760, Oct. 2001.
- [27] A. Gasparri, S. Panzieri, F. Pascucci and G. Ulivi, "A Hybrid Active Global Localisation Algorithm for Mobile Robots," *Proceedings 2007 IEEE International Conference on Robotics and Automation*, Rome, Italy, 2007, pp. 3148-3153.
- [28] A. C. Murtra, J. M. Mirats Tur and A. Sanfeliu, "Efficient active global localization for mobile robots operating in large and cooperative environments," 2008 IEEE International Conference on Robotics and Automation, Pasadena, CA, USA, 2008, pp. 2758-2763.
- [29] Y. Wang, W. Chen, J. Wang, and H. Wang, "Active global localization based on localizability for mobile robots," *Robotica*, vol. 33, no. 8, pp. 1609–1627, 2015.
- [30] K. P. Cop, P. V. K. Borges and R. Dubé, "Delight: An Efficient Descriptor for Global Localisation Using LiDAR Intensities," 2018 IEEE International Conference on Robotics and Automation (ICRA), Brisbane, QLD, Australia, 2018, pp. 3653-3660.
- [31] J. Meng et al., "Efficient and Reliable LiDAR-Based Global Localization of Mobile Robots Using Multiscale/Resolution Maps," in IEEE Transactions on Instrumentation and Measurement, vol. 70, pp. 1-15, 2021.
- [32] A. Filotheou, A. Tzitzis, E. Tsardoulias, A. Dimitriou, A. Symeonidis, G. Sergiadis, and L. Petrou, "Passive global localisation of mobile robot via 2D Fourier-Mellin invariant matching," *Journal of Intelligent & Robotic Systems*, vol. 104, no. 2, p. 26, 2022.
- [33] A. Filotheou, "CBGL: Fast Monte Carlo Passive Global Localisation of 2D LIDAR Sensor," 2024 IEEE/RSJ International Conference on Intelligent Robots and Systems (IROS), Abu Dhabi, United Arab Emirates, 2024, pp. 3268-3275.
- [34] R. B. Rusu and S. Cousins, "3D is here: Point Cloud Library (PCL)," 2011 IEEE International Conference on Robotics and Automation, Shanghai, China, 2011, pp. 1-4.